REPORT

www.the-innovation.org

Magnetic-field modulation of topological electronic state and emergent magneto-transport in a magnetic Weyl semimetal

Jianlei Shen,[1,2,8] Jiacheng Gao,[1,3,8] Changjiang Yi,[1,8] Meng Li,[1,3,8] Shen Zhang,[1,3] Jinying Yang,[1,3] Binbin Wang,[1] Min Zhou,[4] Rongjin Huang,[4] Hongxiang Wei,[1] Haitao Yang,[1] Youguo Shi,[1,5] Xiaohong Xu,[2] Hong-Jun Gao,[1,5] Baogen Shen,[1,3,6,7] Geng Li,[1,5,*] Zhijun Wang,[1,3,*] and Enke Liu[1,5,*]

*Correspondence: gengli.iop@iphy.ac.cn (G.L.); wzj@iphy.ac.cn (Z.W.); ekliu@iphy.ac.cn (E.L.)

Received: December 1, 2022; Accepted: February 14, 2023; Published Online: February 20, 2023; https://doi.org/10.1016/j.xinn.2023.100399

GRAPHICAL ABSTRACT

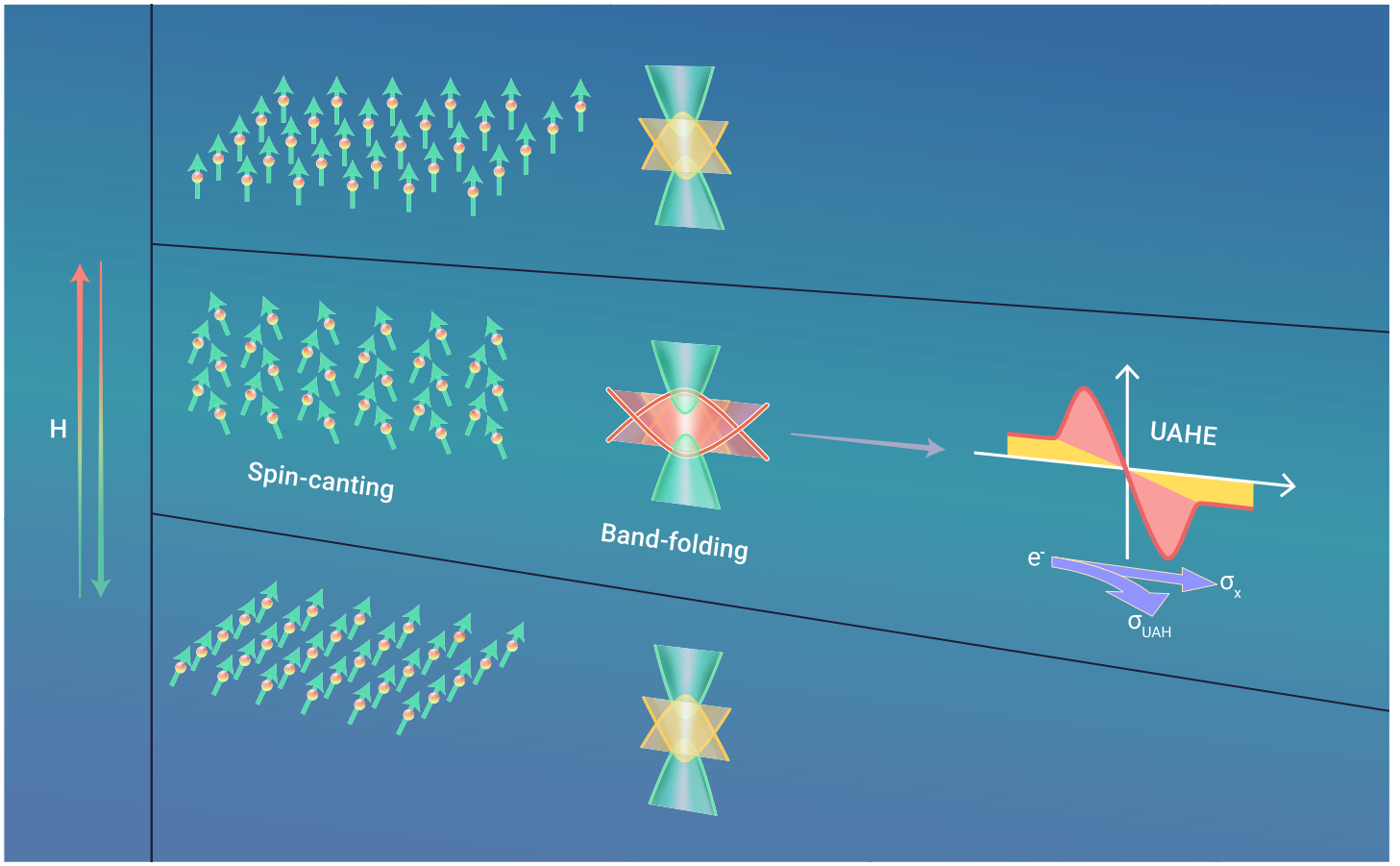

PUBLIC SUMMARY

- Modulation of Weyl electronic state by external field is highly desired.
- Weyl electronic state and transverse transport are synchronously modulated.
- Such modulation is realized by magnetic field-induced spin canting.
- Non-collinear magnetism and topological electronic state can be connected.

REPORT

Magnetic-field modulation of topological electronic state and emergent magneto-transport in a magnetic Weyl semimetal

Jianlei Shen,[1,2,8] Jiacheng Gao,[1,3,8] Changjiang Yi,[1,8] Meng Li,[1,3,8] Shen Zhang,[1,3] Jinying Yang,[1,3] Binbin Wang,[1] Min Zhou,[4] Rongjin Huang,[4] Hongxiang Wei,[1] Haitao Yang,[1] Youguo Shi,[1,5] Xiaohong Xu,[2] Hong-Jun Gao,[1,5] Baogen Shen,[1,3,6,7] Geng Li,[1,5,*] Zhijun Wang,[1,3,*] and Enke Liu[1,5,*]

[1]Beijing National Laboratory for Condensed Matter Physics, Institute of Physics, Chinese Academy of Sciences, Beijing 100190, China

[2]Key Laboratory of Magnetic Molecules and Magnetic Information Materials of Ministry of Education & Research Institute of Materials Science, Shanxi Normal University, Taiyuan 030000, China

[3]School of Physical Sciences, University of Chinese Academy of Sciences, Beijing 100049, China

[4]Key Laboratory of Cryogenics, Technical Institute of Physics and Chemistry, Chinese Academy of Sciences, Beijing 100190, China

[5]Songshan Lake Materials Laboratory, Dongguan 523808, China

[6]Ningbo Institute of Materials Technology & Engineering, Chinese Academy of Sciences, Ningbo, Zhejiang 315201, China

[7]Ganjiang Innovation Academy, Chinese Academy of Sciences, Ganzhou, Jiangxi 341000, China

[8]These authors contributed equally

*Correspondence: gengli.iop@iphy.ac.cn (G.L.); wzj@iphy.ac.cn (Z.W.); ekliu@iphy.ac.cn (E.L.)

Received: December 1, 2022; Accepted: February 14, 2023; Published Online: February 20, 2023; https://doi.org/10.1016/j.xinn.2023.100399

Citation: Shen J., Gao J., Yi C., et al., (2023). Magnetic-field modulation of topological electronic state and emergent magneto-transport in a magnetic Weyl semimetal. The Innovation **4(2)**, 100399.

The modulation of topological electronic state by an external magnetic field is highly desired for condensed-matter physics. Schemes to achieve this have been proposed theoretically, but few can be realized experimentally. Here, combining transverse transport, theoretical calculations, and scanning tunneling microscopy/spectroscopy (STM/S) investigations, we provide an observation that the topological electronic state, accompanied by an emergent magneto-transport phenomenon, was modulated by applying magnetic field through induced non-collinear magnetism in the magnetic Weyl semimetal EuB_6. A giant unconventional anomalous Hall effect (UAHE) is found during the magnetization re-orientation from easy axes to hard ones in magnetic field, with a UAHE peak around the low field of 5 kOe. Under the reasonable spin-canting effect, the folding of the topological anti-crossing bands occurs, generating a strong Berry curvature that accounts for the observed UAHE. Field-dependent STM/S reveals a highly synchronous evolution of electronic density of states, with a d*I*/d*V* peak around the same field of 5 kOe, which provides evidence to the folded bands and excited UAHE by external magnetic fields. This finding elucidates the connection between the real-space non-collinear magnetism and the *k*-space topological electronic state and establishes a novel manner to engineer the magneto-transport behaviors of correlated electrons for future topological spintronics.

INTRODUCTION

From the perspective of applications of spintronics and future quantum devices, it is highly desirable to modulate the electronic structures using external fields and further to control the electronic transport behavior. Recently, materials with topologically non-trivial electronic states have attracted much attention.[1–4] In particular, magnetic topological materials,[5–9] where the transport behavior, such as the intrinsic anomalous Hall effect (AHE),[5,6,10] anomalous Nernst effect,[11,12] and quantum AHE,[9,13] are dominated by subtle topological electronic bands near the Fermi level. Therefore, magnetic topological materials have emerged as an ideal platform for relating the transport behavior and electronic structures in the external fields.

It is known that the electronic structures can be significantly influenced by the spin configuration by breaking or preserving the mirror symmetry.[14] Therefore, modulating the spin structure using a magnetic field is a potential strategy for realizing the modulation of topological bands. According to the existing theories and experiments, two main effects of the magnetic field modulating the topological state are the movement of Weyl nodes and the generation of a topological state. Theoretical calculations have predicted that the position of the Weyl nodes could be manipulated through magnetization rotation and Zeeman splitting during the magnetization process, resulting in varying AHEs.[15–18] In addition, the mixing of electronic bands with equal or opposite spin owing to spin-orbit coupling (SOC) was proposed based on the spin-canting effect, resulting in a non-linear geometrical Hall effect.[19] However, there is no solid experimental evidence for the studies mentioned above, and the related physical mechanism is still being developed. Therefore, further studies are essential.

EuB_6, which has a simple band structure (see supplemental information and Figures S1 and S2), was recently predicted to be a magnetic topological semimetal.[20–22] According to the magnetic symmetry of the system, EuB_6 could be a nodal-line semimetal or a Weyl semimetal.[19] Moreover, a topological phase transition across the curie temperature was confirmed using angle-resolved photoemission spectroscopy and magneto-Kerr effect microscopy.[21,22] The magnetization measurements showed two magnetic transitions at 15.3 and 12.5 K, corresponding to the magnetic moments along the [100] and [111] directions, respectively.[23] The theoretically calculated magneto-crystalline anisotropy energy of EuB_6 was only 8 meV,[20] which indicated that the orientation of the magnetic moments could be easily driven by a magnetic field. In this case, the magnetic field controlling the spin orientation in real space changed the mirror symmetry of the system and affected the topological band structures in momentum space. Therefore, the magnetic Weyl semimetal EuB_6 is a potentially ideal system for modulating the topological bands using a magnetic field.

Here, by combining transport measurements, theoretical calculations, and scanning tunneling microscopy/spectroscopy (STM/S), we present strong evidence that the magnetic field can significantly modulate the topological bands and further produce unconventional transport behavior through the field-induced spin-canting effect in magnetic Weyl semimetal EuB_6.

RESULTS AND DISCUSSION

EuB_6 crystallizes in a CaB_6 structure with a space group of 221 (Figure 1A). Two significant magnetic transition temperatures, T_{C1} and T_{C2}, can be observed in inset of Figure 1C, which indicates that the spin orientation changes from the [100] to the [111] direction as the temperature decreases and that the easy axis is in the [111] direction[23] (see also Figure 1A). Figure 1D shows the magnetic field dependence of isothermal *M* (top panel) and Hall resistivity ρ_{yx} (bottom panel) at 2 K. The magnetization curves for *H* along the [100], [110], and [111] directions exhibited weak magneto-crystalline anisotropy. The dashed lines shown in Figure 1D (bottom panels) represent the linear fit of ρ_{yx} above saturation field H_S. In the case of *H*//[100] and [111], the dashed lines did not pass through the original point at 2 K, indicating the existence of the conventional AHE (CAHE). However, in the case of *H*//[110] the dashed line did pass through the original point, meaning that the CAHE is unobvious. Interestingly, an additional component of AHE was unexpectedly observed before H_S for *H*//[100] and [110]. A significant Hall resistivity peak, referred to as an unconventional AHE (UAHE; ρ_{yx}^{UA}), emerged before the magnetization saturation of the system. With increasing temperature, ρ_{yx}^{UA} became weaker and vanished, and only the CAHE remained (see supplemental information and Figure S3). Notably, a very small UAHE for *H*//[111] was attributed to the inevitable direction tilt during the cutting of the single crystals. In addition, the large negative magneto-resistance was observed in three directions (see supplemental information and Figure S4).

In general, the total Hall resistivity is expressed as $\rho_{yx} = R_0H + R_sM + \rho_{yx}^{UA}$, where the three terms on the right of the equation are the normal Hall term, the conventional anomalous Hall term, and the unconventional anomalous Hall term. Based on ρ_{yx} measurement data, the high field part is the linear normal

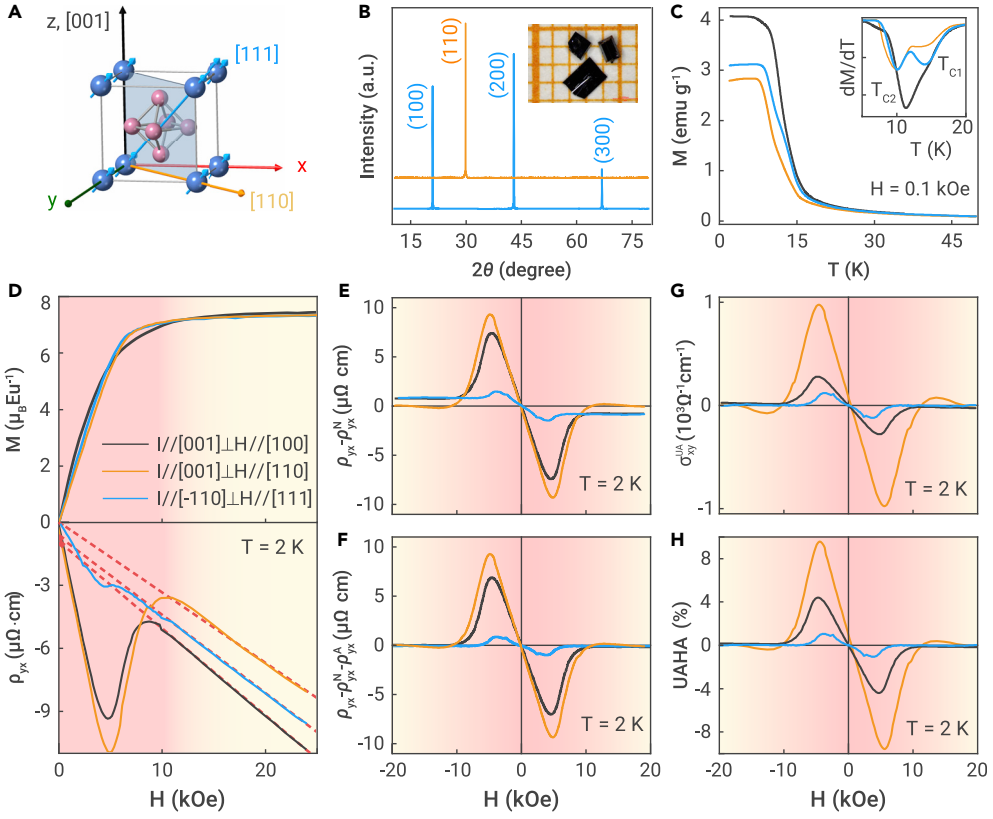

Figure 1. Structural, magnetic, and unconventional transport properties (A) Crystal structure of EuB_6. Blue arrows indicates that the magnetic moments are along the [111] direction at ground state. (B) Room temperature XRD patterns of single crystalline samples. The inset shows the optical morphology of single crystals. (C) Temperature dependence of M with the field cooling model for H = 0.1 kOe along [100], [110], and [111]. Inset shows the temperature dependence of dM/dT. (D) Magnetic field dependence of isothermal M (top panel) and Hall resistivity ρ_{yx} (bottom panel) at 2 K for H along [100], [110], and [111], respectively. (E) Anomalous Hall resistivity $\rho_{yx}^{A} = \rho_{yx} - \rho_{yx}^{N}$ at 2 K as a function of the magnetic field H for I//[−110], [001], and [001] and H//[111], [100], and [110], where $\rho_{yx}^{N} = R_0H$ is the ordinary Hall term. (F) Unconventional anomalous Hall resistivity ($\rho_{yx}^{UA} = \rho_{yx} - \rho_{yx}^{N} - \rho_{yx}^{A}$) at 2 K. (G and H) Unconventional anomalous Hall conductivity (σ_{xy}^{UA}) and unconventional anomalous Hall angle (UAHA) at 2 K.

Hall term $\rho_{yx}^{N} = R_0H$, and the total anomalous Hall term, which includes the CAHE and UAHE, can be extracted based on $\rho_{yx}^{A} = \rho_{yx} - \rho_{yx}^{N}$, as shown in Figure 1E. The CAHE and UAHE were obtained at 2 K for H along the [100] and [111] directions, while only UAHE was obtained for H along the [110] direction (also see Figure 1D). For H along [100] and [111], the conventional ρ_{yx}^{A} was only 0.65 μΩ cm at 2 K above H_S. To obtain ρ_{yx}^{UA} below H_S, ρ_{yx}^{UA} is defined as $\rho_{yx}^{UA} = \rho_{yx} - R_0H - R_SM$, where R_S can be determined using the data above H_S by considering $\rho_{yx}^{UA} = 0$ and $M = M_s$ after magnetization saturation. Figure 1F shows the ρ_{yx}^{UA} after subtracting the normal and conventional anomalous Hall terms for H along [100], [110], and [111]. The maximum ρ_{yx}^{UA} values were 4.4, 9.6, and 1.0 μΩ cm under H = 4.7, 5.0, and 3.8 kOe, respectively. Furthermore, the UAHC (σ_{xy}^{UA}) can be calculated by the relation $\sigma_{xy}^{UA}(H) = \rho_{yx}^{UA}(H)/(\rho_{yx}^{UA2}(H) + \rho_{xx}^{2}(H))$. As shown in Figure 1G, for H along [100], [110], and [111], the maximum σ_{xy}^{UA} values were 280, 976, and 120 Ω^{-1} cm^{-1}, respectively. In addition, the unconventional anomalous Hall angle (UAHA) was obtained using the relation $UAHA = \rho_{yx}^{UA}/\rho_{xx}$, as shown in Figure 1H. The maximum UAHA values were 4.4%, 9.6%, and 1% for [100], [110], and [111], respectively. The UAHE in EuB_6 is much larger than the CAHE and is also larger than that for many ferromagnetic (FM) systems.[24–29]

The UAHE is very similar to the topological Hall effect (THE) in materials with topological spin textures in real space,[30–33] in which the Dzyaloshinskii-Moriya interaction (DMI) plays an important role. However, it is considered that DMI does not exist in centrosymmetric EuB_6. Therefore, the UAHE in EuB_6 most likely results from the evolution of the Berry curvature in momentum space. A similar electronic structure analysis was also performed in the magnetic Weyl semimetal $EuCd_2As_2$.[34] For EuB_6, a very low magneto-crystalline anisotropy energy of 8 meV was reported in a previous theoretical study.[20] This indicates that the competition between the magneto-crystalline anisotropy energy and the Zeeman energy gained in the magnetic field balance each other. In this case, the applied magnetic field potentially induced the non-collinear spin canting, which may further alter the topological bands and electronic transport properties of EuB_6. It is also different from the CAHE, which depends on the unchanged magnetism and the electronic structures (Berry curvature). During the magnetizing process, the reverse magnetic domain decreases, and the AHE increases. After the magnetization saturation, both the electronic structures and the CAHE remain unchanged. For the UAHE in EuB_6, in contrast, the spin canting was generated just during the magnetization re-orientation process, which results in an AHE peak with the evolution of topological bands and Berry curvature. The UAHE disappears again after the vanishing of the spin canting above the saturation field. The observation that the ρ_{yx}^{UA} peak was weak when the field was along the [111] easy axis and intense when the field was along [100] and [110] indicated that a possible spin-canting behavior ensues when the external magnetic field deviates from the easy axis.

Based on the deduction of spin canting from the transport results, we performed first-principles calculations to examine the effect of non-collinear magnetism on the electronic structures. Starting from the z-directed FM order, we added in-plane spin components ($m_{//}$) to different Eu atoms (marked in Figure 2C), thereby doubling the size of unit cells along all three lattice vectors. The energy difference was 8 meV when the canting angle θ was 45° ($\tan\theta = m_{//}/m_z$), which indicates that the spin orientations can be easily tuned using external fields. Because of the band-folding effect, the band inversions (consisting of B-p and Eu-d orbits; see supplemental information and Figure S2) appearing at the high-symmetry k-points X, Y, and Z folded to the Γ point. When the canted spin components became zero and the system was FM, 2-fold degenerate bands existed around the Γ point (marked in Figure 2A) because of the band folding owing to the equivalence of the x and y directions. Upon increasing the canted spin components, the degenerated bands split, and all crossings along the Γ-Z path become gapped under SOC, as shown in Figures 2D and 2E. Although the energy scale of the spin-canting-induced band splitting was small (less than 20 meV at the Γ point), the bands changed considerably upon coupling with the previous single degenerate band (green regions in Figures 2D and 2E), leading to an enhancement in the Berry curvature in the coupled area. The Berry curvature can be calculated directly using the linear-response Kubo formula.[35] We calculated the Berry curvature Ω_{xy} along the high-symmetry Γ-Z path, on which Ω_{yz} and Ω_{zx} always have the same value because of the Θm_{-110} symmetry. Each peak in the Berry curvature spectrum corresponds to the band-crossing regime of the band structure. When the canting angle was zero, the bands arising from the high-symmetry k-points X and Y (doubly degenerate bands) did not couple with the bands from the Z point (single degenerate band) (Figure 2F). Owing to the spin-canting effect, these bands couple and open gaps (Figure 2H), which induce two additional peaks in the Berry curvature spectrum (left in Figure 2G). When H was smaller than H_S, the electronic band structure could be modulated by this behavior of the non-collinear magnetism. The folding of the electronic band structure thus resulted in the UAHE during the magnetization process. However, when H was larger than H_S, all moments followed the direction of the external magnetic field, and both the spin-canting effect and the UAHE disappeared, and only the CAHE remained owing to collinear FM. Furthermore, when H exceeded H_S at 2 K, the conventional AHCs measured in our study were only 24 and 89 Ω^{-1} cm^{-1} for [100] and [111], respectively (see supplemental information and Figure S5), which are consistent with the theoretical calculations for the collinear FM state.[20]

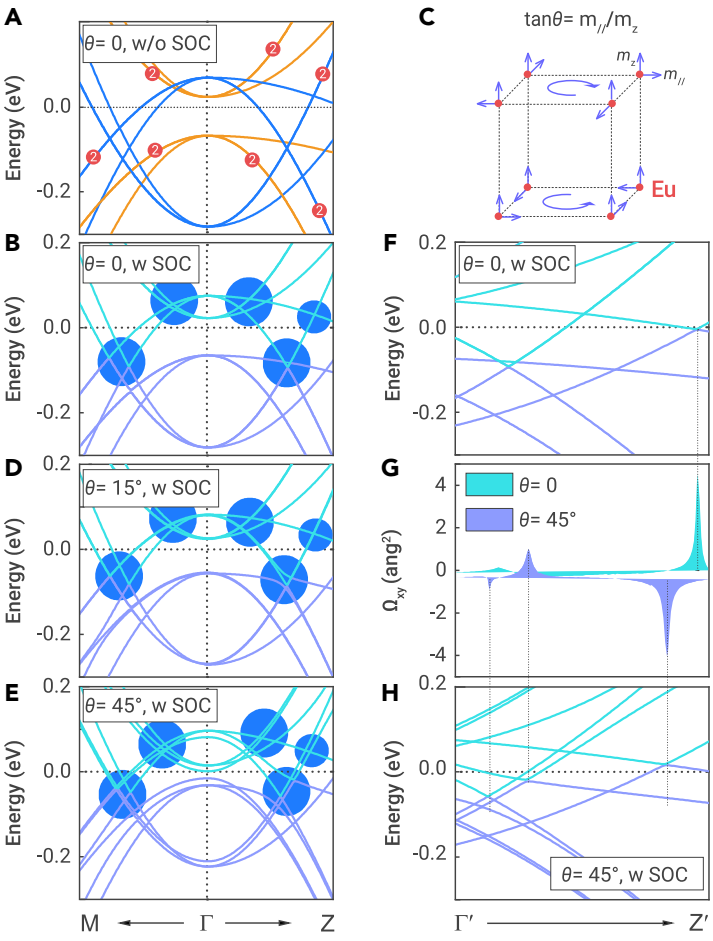

Figure 2. Theoretical calculations on the spin-canting-induced electronic structures
(A) FM-order band structure for enlarged supercell without considering SOC. Blue and yellow lines represent spin-up and spin-down bands, respectively. Doubly degenerate bands are marked specifically. (B) FM-order bands after considering SOC. Cyanine blue and light purple lines represent conduction and valence bands, respectively. (C) Schematic of magnetic orientation on each Eu atom in the supercell. (D and E) Spin-canting band structures with different in-plane magnetic moments for canting angle θ = 15° (D) and 45° (E). (F and H) Band-crossing regime for θ = 0° (F) and 45° (H) along the Γ-Z path. (G) Calculated Berry curvature Ω_{xy} around the band-crossing regime along the Γ-Z path.

When magnetization re-orientation from easy axes to hard ones occurs in EuB_6, the magnetic order of the system could take an intermediate non-linear spin-canting state. This spin-canting state enlarges the magnetic unit cell and lowers the symmetry of system, leading to the folding of the bands and change in local density of states (LDOS), which could be reflected in the variation of d*I*/d*V* spectra in STM/S measurements. To verify the evolution of the band structure with an external magnetic field, we performed low-temperature STM/S studies on the Eu-terminated surface of EuB_6 (see supplemental information and Figure S6). As shown in Figure 3A, the square lattice, which indicates that the surface was cleaved along the (001) crystal plane, was clearly resolved in the high-resolution images. The intensity map of d*I*/d*V* spectra, which are spatially homogeneous within a several-nm scale (see supplemental information and Figure S6), shows uniform distribution of LDOS along the red arrow (Figure 3B). We then applied an external magnetic field perpendicular to the surface and recorded the field-dependent averaged d*I*/d*V* spectra (Figure 3C) along the red arrow in Figure 3A. In this case, the magnetic moments gradually rotated from the [111] easy axis to the [001] axis. Significantly, the line shapes of the spectra show a strong field dependence at small magnetic field. In EuB_6, the saturated magnetic field is about 10 kOe along the [001] direction. Thus, the response of d*I*/d*V* spectra to the magnetic field happens only below 10 kOe. After the magnetic moment saturates (>10 kOe) along the [001] direction, no remarkable variation in LDOS is observed upon further increase of the magnetic field. Notably, this field-dependent evolution in the LDOS occurred in a rather broad energy window, suggesting a possible reconstruction of the topological band structures.

We further extracted the field-dependent intensity of the spectra in Figure 3C and plotted the intensity values in a series of energies as a function of the magnetic field in Figure 3D. For all energy cuts, the intensity of the d*I*/d*V* spectrum showed an initial increase, peaked at approximately 5 kOe, and then gradually decreased as the field reached H_S. This observation is reminiscent of the transport measurements (Figures 1D–1H), where the UAHE demonstrates a highly concurrent field dependence, with an exact same maximum at 5 kOe. The spin-canting effect causes the band folding and changes the DOS near the Fermi level (Figures 2D, 2E, 3C, and 3D), which further leads to the UAHE. We plotted the intensity map (Figure 3E) of the negative second derivative of the spectra in Figure 3C, and the field-dependent STS features could be observed more clearly. The substantial enhancement of negative second derivative during the magnetization indicates a change in LDOS of EuB_6 with the application of external magnetic field.

To provide a clear physical picture, a schematic of the modulation of the electronic band structure and transverse electronic transport characteristics of the magnetic Weyl semimetal EuB_6 during the entire magnetization process is shown in Figure 4. According to the magnetic measurement results, the ground-state magnetic moment of EuB_6 aligns with the [111] easy axis (Figures 4A and 4B). For *H*//[111], there are no spin-canting and band-folding effects during the entire magnetization process. Therefore, it only shows the CAHE upon the unchanged topological bands, as shown in the top part of Figures 4B–4E. As long as the moments deviate from the easy axis to the hard axis, the competition between the magneto-crystalline anisotropy and the external magnetic field leads to the spin canting, which results in a band-folding effect in momentum space, leading to splitting of the pristine bands and production of additional bands, as shown by the red color in the middle and bottom regions of Figure 4C. With the aid of split bands and SOC-induced anti-crossings, an enhancement of the Berry curvature can be obtained. For *H* along the [100] and [110] main directions, the enhanced Berry curvature leads to the large UAHE during the magnetization process. Once the system enters the saturation state of magnetization, both spin canting and band folding disappear again, as shown in the middle and bottom regions of Figure 4D. Therefore, the UAHE vanishes, and the CAHE produced by the linear FM state remains, as shown in Figure 4E. This implies that as long as the magnetic field deviates from the [111] easy axis in EuB_6, a dynamic picture of spin canting, band folding, and the UAHE during the process of magnetization and demagnetization is very likely to be observed.

In current studies, the peak of the Hall sign during the magnetization process was widely considered to be THE, attributed to the topological spin structures in real space.[30–33] In our study, we observed band splitting and LDOS evolution, resulting in a prominent UAHE. An external field can change the magnetic structure and further modulate the topological electronic structures, revealing an interplay between the magnetism and topology. The physical origin of the observed Hall peaks during the magnetization process can also be ascribed to the alteration of topological electronic structure in momentum space, not only the topological spin structure in real space.

CONCLUSION

In summary, the topological electronic structure was modulated owing to the spin-canting effect in magnetic Weyl semimetal EuB_6 during the magnetization re-orientation with the application of a magnetic field. An emergent UAHE was observed with a maximum UAHC of approximately 1,000 Ω^{-1} cm^{-1} and a UAHA of approximately 10% at a low field of 5 kOe. Combining the experiments and theory, we present strong evidence that the magnetic field significantly modulates the topological electronic state and the unconventional transport behavior. Our findings provide not only an insight into the relationship between the magnetic and electronic structures but also guidance for manipulating the electronic transport properties through the external magnetic field, particularly in emergent magnetic correlated electronic materials for topological spintronics.

MATERIALS AND METHODS

Sample preparation and physical property measurements

EuB_6 single crystals were prepared using the flux method. The ingredients with a ratio of Eu:B:Al = 1:8:100 were placed in an alumina crucible and heated to 1,773 K in a furnace under an atmosphere of high-purity argon. Subsequently, the furnace was slowly cooled to 1,573 K

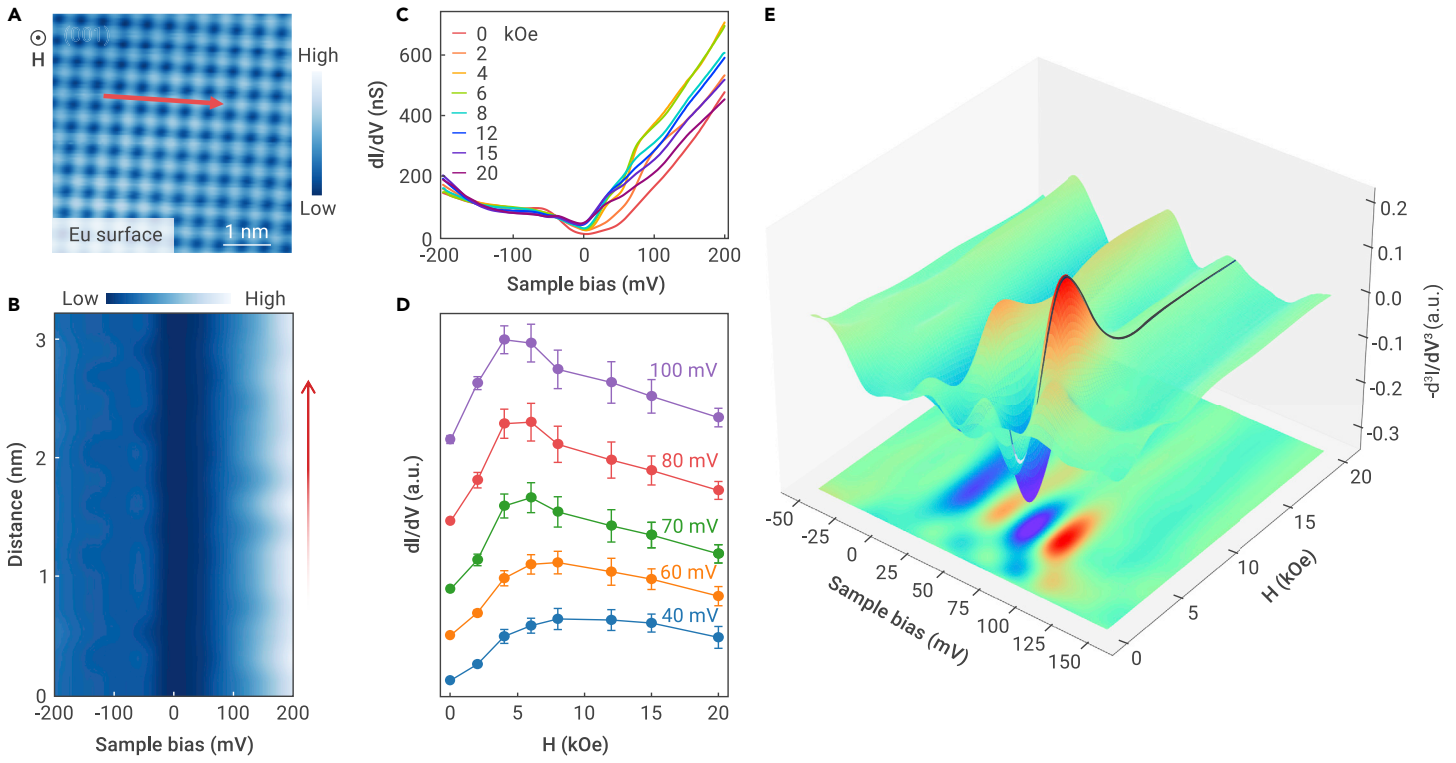

Figure 3. Field-dependent STM/S characterization on the electronic state (A) Atomically resolved image of the Eu-terminated (001) surface, showing the square Eu lattice. The applied magnetic field is perpendicular to the (001) surface. Scanning settings: bias V_s = −200 mV, setpoint I_t = 200 pA. (B) Intensity map of 15 d*I*/d*V* spectra taken along the red arrow in (A) under zero magnetic field. (C) Field-dependent d*I*/d*V* spectra taken under magnetic fields from 0 to 20 kOe. Each spectrum is the average of 15 spectra taken along the red arrow in (A) but under different magnetic fields. Setpoint current of each spectrum is kept the same at 200 pA. (D) Intensity plot of the spectra in (C) under different energies as a function of the magnetic fields. The errors come from the standard deviations of 15 different spectra taken along the red arrow in (A). (E) Intensity plot of the negative second derivative of the spectra in (C). The second derivative of d*I*/d*V* is used to make the subtle features in the d*I*/d*V* spectra more pronounced. All the STM/S measurements are taken under 0.45 K.

at a rate of 2 K/h and then rapidly cooled to room temperature at a rate of 200 K/h. Single-crystalline samples were obtained and then washed with sodium hydroxide solution and deionized water and present with a black cubic shape (see inset in Figure 1B). The crystal structure of single-crystal samples was characterized by X-ray diffraction (XRD). Room temperature XRD patterns of EuB_6 show only the (*h*00) and (*hk*0) Bragg peaks, which indicate that the two exposed surfaces are the (100) and (110) planes, as shown in Figure 1B. Magnetic properties were measured by a superconducting quantum interference device (SQUID) magneto-meter. Electric transport properties were measured by the physical property measurement system (PPMS).

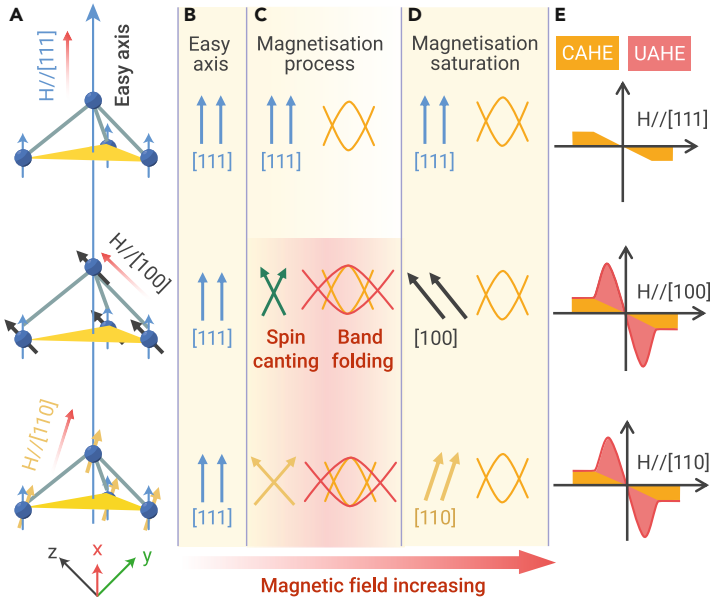

Figure 4. Physical picture of relation between non-collinear magnetism and the unconventional transport behavior (A) Magnetic fields along [111], [100], and [110] directions and the rotations of the magnetic moments. (B) Magnetic moments along [111] easy axis in the ground state below T_{C2}. (C) Spin-canting and band-folding effects in the low-field magnetization process for *H* along [100] and [110]. There are no spin-canting and band-folding effects for *H* along [111] easy axis. (D) Magnetic moments along the external magnetic field and corresponding electronic bands for saturated magnetization. Spin-canting and band-folding effects disappear again in this case. (E) CAHE and UAHE for *H* along different crystal axes. Red arrow at the bottom indicates the increasing magnetic field along the main crystal axes.

STM/S measurements

EuB_6 single crystals were mounted on the metal sample holders by conductive epoxy. The crystals were mechanically cleaved under 12 K and then immediately transferred to the STM scanner (Unisoku). STM/S measurements were performed under 0.45 K. The differential conductance (d*I*/d*V*) spectra were obtained with a standard lock-in amplifier at a frequency of 973.0 Hz, with a modulation voltage of 0.2 mV. Magnetic fields were applied perpendicular to the samples.

First-principles calculations

First-principles calculations were performed with the Vienna *ab-initio* simulation package (VASP) based on the density functional theory (DFT) with the projector augmented wave (PAW) method.[36–39] The exchange-correlation potential is treated using the generalized gradient approximation (GGA) parametrized by Perdew, Burke, and Ernzerhof (PBE).[40] The rotationally invariant on-site coulomb interactions on 4*f* electrons are taken to be 8 eV. For the non-collinear magnetic calculations, the 400 eV energy cutoff and the 4 × 4 × 4 Γ-centered *k*-mesh are adopted in the self-consistent calculations. The momentum-dependent Berry curvature is calculated according to the following Kubo formula:

$$\Omega_{n,\alpha\beta} = -2Im\sum_{m\neq n}\frac{\upsilon_{nm,\alpha}(k)\upsilon_{nm,\beta}(k)}{[\omega_m(k)-\omega_n(k)]^2}.$$

The velocity operators are calculated by using the PAW wave functions as proposed in Song et al.[41]

$$V_{nm,\alpha}(k) = \frac{1}{\hbar}\langle u_{nk}\left|\frac{\partial H(k)}{\partial k_\alpha}\right|u_{mk}\rangle$$

In the Berry curvature calculations, we take 280 valence bands and 220 conduction bands to ensure the convergence.

REFERENCES

1. Weng, H., Fang, C., Fang, Z., et al. (2015). Weyl semimetal phase in noncentrosymmetric transition-metal monophosphides. Phys. Rev. X ***5***, 011029.
2. Huang, S.M., Xu, S.Y., Belopolski, I., et al. (2015). A Weyl Fermion semimetal with surface Fermi arcs in the transition metal monopnictide TaAs class. Nat. Commun. ***6***, 7373.
3. Soluyanov, A.A., Gresch, D., Wang, Z., et al. (2015). Type-II weyl semimetals. Nature ***527***, 495–498.
4. Sun, Y., Wu, S.C., Ali, M.N., et al. (2015). Prediction of Weyl semimetal in orthorhombic $MoTe_2$. Phys. Rev. B ***92***, 161107.
5. Liu, E., Sun, Y., Kumar, N., et al. (2018). Giant anomalous Hall effect in a ferromagnetic kagome-lattice semimetal. Nat. Phys. ***14***, 1125–1131.
6. Wang, Q., Xu, Y., Lou, R., et al. (2018). Large intrinsic anomalous Hall effect in half-metallic ferromagnet $Co_3Sn_2S_2$ with magnetic Weyl fermions. Nat. Commun. ***9***, 3681.
7. Liu, D.F., Liang, A.J., Liu, E.K., et al. (2019). Magnetic Weyl semimetal phase in a Kagomé crystal. Science ***365***, 1282–1285.
8. Morali, N., Batabyal, R., Nag, P.K., et al. (2019). Fermi-arc diversity on surface terminations of the magnetic Weyl semimetal $Co_3Sn_2S_2$. Science ***365***, 1286–1291.
9. Deng, Y., Yu, Y., Shi, M.Z., et al. (2020). Quantum anomalous Hall effect in intrinsic magnetic topological insulator $MnBi_2Te_4$. Science ***367***, 895–900.
10. Shen, J., Yao, Q., Zeng, Q., et al. (2020). Local disorder-induced elevation of intrinsic anomalous Hall conductance in an electron-doped magnetic Weyl semimetal. Phys. Rev. Lett. ***125***, 086602.
11. Guin, S.N., Vir, P., Zhang, Y., et al. (2019). Zero-field Nernst effect in a ferromagnetic kagome-lattice weyl-semimetal $Co_3Sn_2S_2$. Adv. Mater. ***31***, 201806622.
12. Yang, H., You, W., Wang, J., et al. (2020). Giant anomalous Nernst effect in the magnetic Weyl semimetal $Co_3Sn_2S_2$. Phys. Rev. Mater. ***4***, 024202.
13. Howard, S., Jiao, L., Wang, Z., et al. (2021). Evidence for one-dimensional chiral edge states in a magnetic Weyl semimetal $Co_3Sn_2S_2$. Nat. Commun. ***12***, 4269.
14. Noky, J., Xu, Q., Felser, C., and Sun, Y. (2019). Large anomalous Hall and Nernst effects from nodal line symmetry breaking in Fe_2MnX (X = P, As, Sb). Phys. Rev. B ***99***, 165117.
15. Ghimire, M.P., Facio, J.I., You, J.S., et al. (2019). Creating Weyl nodes and controlling their energy by magnetization rotation. Phys.Rev. Res. ***1***, 032044.
16. Takahashi, K.S., Ishizuka, H., Murata, T., et al. (2018). Anomalous Hall effect derived from multiple Weyl nodes in high-mobility $EuTiO_3$ films. Sci. Adv. ***4***, eaar7880.
17. Li, P., Koo, J., Ning, W., et al. (2020). Giant room temperature anomalous Hall effect and tunable topology in a ferromagnetic topological semimetal Co_2MnAl. Nat. Commun. ***11***, 3476.
18. Wang, P., Ge, J., Li, J., et al. (2021). Intrinsic magnetic topological insulators. The Innovation ***2***, 100098.
19. Hirschberger, M., Nomura, Y., Mitamura, H., et al. (2021). Geometrical Hall effect and momentum-space Berry curvature from spin-reversed band pairs. Phys. Rev. *B* ***103***, L041111.
20. Nie, S., Sun, Y., Prinz, F.B., et al. (2020). Magnetic semimetals and quantized anomalous Hall effect in EuB_6. Phys. Rev. Lett. ***124***, 076403.
21. Gao, S., Xu, S., Li, H., et al. (2021). Time-reversal symmetry breaking driven topological phase transition in EuB_6. Phys. Rev. X ***11***, 021016.
22. Liu, W.L., Zhang, X., Nie, S.M., et al. (2022). Spontaneous ferromagnetism induced topological phase transition in EuB_6. Phys. Rev. Lett. ***129***, 166402.
23. Süllow, S., Prasad, I., Aronson, M.C., et al. (1998). Structure and magnetic order of EuB_6. Phys. Rev. B ***57***, 5860–5869.
24. Fang, Z., Nagaosa, N., Takahashi, K.S., et al. (2003). The anomalous Hall effect and magnetic monopoles in momentum space. Science ***302***, 92–95.
25. Wu, F., Sajitha, E.P., Mizukami, S., et al. (2010). Electrical transport properties of perpendicular magnetized Mn-Ga epitaxial films. Appl. Phys. Lett. ***96***, 042505.
26. Kim, K., Seo, J., Lee, E., et al. (2018). Large anomalous Hall current induced by topological nodal lines in a ferromagnetic van der Waals semimetal. Nat. Mater. ***17***, 794–799.
27. Miyasato, T., Abe, N., Fujii, T., et al. (2007). Crossover behavior of the anomalous Hall effect and anomalous Nernst effect in itinerant ferromagnets. Phys. Rev. Lett. ***99***, 086602.
28. Nayak, A.K., Fischer, J.E., Sun, Y., et al. (2016). Large anomalous Hall effect driven by a nonvanishing Berry curvature in the noncolinear antiferromagnet Mn_3Ge. Sci. Adv. ***2***, e1501870.
29. Nakatsuji, S., Kiyohara, N., and Higo, T. (2015). Large anomalous Hall effect in a non-collinear antiferromagnet at room temperature. Nature ***527***, 212–215.
30. Neubauer, A., Pfleiderer, C., Binz, B., et al. (2009). Topological Hall effect in the A phase of MnSi. Phys. Rev. Lett. ***102***, 186602.
31. Kanazawa, N., Onose, Y., Arima, T., et al. (2011). Large topological Hall effect in a short-period helimagnet MnGe. Phys. Rev. Lett. ***106***, 156603.
32. Wang, W., Zhang, Y., Xu, G., et al. (2016). A centrosymmetric hexagonal magnet with superstable biskyrmion magnetic nanodomains in a wide temperature range of 100-340 K. Adv. Mater. ***28***, 6887–6893.
33. Hou, Z., Ren, W., Ding, B., et al. (2017). Observation of various and spontaneous magnetic skyrmionic bubbles at room temperature in a frustrated kagome magnet with uniaxial magnetic anisotropy. Adv. Mater. ***29***, 1701144.
34. Cao, X., Yu, J.X., Leng, P., et al. (2022). Giant nonlinear anomalous Hall effect induced by spin-dependent band structure evolution. Phys. Rev. Research ***4***, 023100.
35. Thouless, D.J., Kohmoto, M., Nightingale, M.P., et al. (1982). Quantized Hall conductance in a two-dimensional periodic potential. Phys. Rev. Lett. ***49***, 405–408.
36. Kresse, G., and Furthmüller, J. (1996). Efficiency of ab-initio total energy calculations for metals and semiconductors using a plane-wave basis set. Comput. Mater. Sci. ***6***, 15–50.
37. Kresse, G., and Furthmüller, J. (1996). Efficient iterative schemes for ab initio total-energy calculations using a plane-wave basis set. Phys. Rev. B Condens. Matter ***54***, 11169–11186.
38. Blöchl, P. (1994). Projector augmented-wave method. Phys. Rev. B Condens. Matter ***50***, 17953–17979.
39. Kresse, G., and Joubert, D. (1999). From ultrasoft pseudopotentials to the projector augmented-wave method. Phys. Rev. B ***59***, 1758–1775.
40. Perdew, J., Burke, K., and Ernzerhof, M. (1996). Generalized gradient approximation made simple. Phys. Rev. Lett. ***77***, 3865–3868.
41. Song, Z.Z., Sun, S.S., Xu, Y.Y., et al. (2019). First principle calculation of the effective Zeeman's couplings in topological materials. Preprint at arXiv.

ACKNOWLEDGMENTS

This work was supported by the National Key R&D Program of China (nos. 2022YFA1403800, 2022YFA1403400, and 2019YFA0704900); the Fundamental Science Center of the National Natural Science Foundation of China (no. 52088101); the Synergetic Extreme Condition User Facility (SECUF); the Beijing Natural Science Foundation (no. Z190009); the National Natural Science Foundation of China (nos. 11974394, 12174426, 12104280, and 12004416); the Strategic Priority Research Program (B) of the Chinese Academy of Sciences (CAS) (XDB33000000); the Key Research Program of CAS (no. ZDRW-CN-2021-3); the CAS Project for Young Scientists in Basic Research (YSBR-003); the Scientific Instrument Developing Project of CAS (no. ZDKYYQ20210003); and the Basic Research Plan of Shanxi Province (no. 20210302124160).

AUTHOR CONTRIBUTIONS

E.L. designed research; J.S., S.Z., and J.Y. performed transport measurements. J.G. and Z.W. carried out DFT calculations. C.Y. and Y.S. grew crystals. M.L. and G.L. performed STM/S characterizations with the guidance of H.-J.G. All authors participated in analyzing the data. J.S. and E.L. wrote the paper. E.L. is responsible for project direction, planning and infrastructure.

DECLARATION OF INTERESTS

The authors declare no competing interests.

SUPPLEMENTAL INFORMATION

It can be found online at https://doi.org/10.1016/j.xinn.2023.100399.

LEAD CONTACT WEBSITE

Enke Liu: http://english.iop.cas.cn/pe/?id=933.